Research Article Vol. 27, No. 22 / 28 October 2019 / *Optics Express* 31348

Optics EXPRESS

Spaceborne limb hyperspectral imager for ozone profile detection

QINGSHENG XUE,[1,*] BAI YANG,[1] ZHONGTIAN TIAN,[1] FUPENG WANG,[1] XIAONING LUAN,[1] BING MU,[1] AND SHURONG WANG[2]

[1] *College of Information Science and Engineering, Ocean University of China, Qingdao, Shandong 266100, China*

[2] *Changchun Institute of Optics, Fine Mechanics and Physics, Chinese Academy of Sciences, Changchun 130033, China*

[*] *xueqingsheng@ouc.edu.cn*

Abstract: A spaceborne limb hyperspectral imager for ozone detection is designed and developed. The hyperspectral imager can provide the limb hyperspectral radiances images with wide-band and large dynamic range. It is composed of an off-axis parabolic telescope and prism dispersive off-axis aspheric spectrometer, and large dynamic range detection can be realized by using a band-attenuation filter. The spectral range is from 280nm to 1000nm, the field of view is 2.4° (limb vertical direction) × 0.02° (horizontal direction), and the focal length is 69mm. The design results meet the requirements of image quality and have the characteristics of small volume and light weight, thereby making it especially suitable for the application of space remote sensing unlike existing methods that utilize complicated scanning mirror and multiple color separators. The limb hyperspectral imager is measured and calibrated on ground. It detected limb hyperspectral radiances on Tiangong-2 spacecraft of China.

1. Introduction

The atmosphere is an important part of the earth's climate and environment and directly affects the weather and the environment. Apart from the oceans and the biosphere, the atmosphere is also considerably influenced by solar activities. Earth and space scientists have focused mainly on detecting and understand the overall behavior and interaction of the atmosphere. Through atmospheric detection, the density of the entire atmosphere, the vertical distribution of ozone and aerosols, and the changes and disturbance in the state of the middle atmosphere can be understood. Earth sciences, space physics, and environmental studies on global change should determine the scientific significance and understand the process of atmospheric and low-level interactions. A dynamic atmosphere model should also be established and verified to understand the relationship among solar activity, space weather, and earth weather [1–2]. Ozone is a trace gas that plays an important role in the atmospheric climate and environment. Ozone is a key factor of climate change and an important oxidizer in atmospheric photochemistry. Ozone in the stratosphere blocks ultraviolet (UV) rays from the sun, thereby protecting life on earth. In the troposphere, ozone is one of the main pollutant gases. The distribution and change of ozone must be observed continuously to understand the emission and distribution characteristics of air pollution sources and predict the components of air [3–4]. Limb ozone profile detection based on limb scattering measurement technology is an important method of spaceborne ozone detection. Its principle involves ultraviolet(UV), visible (VIS), and near infrared (NIR) spectral range in measuring solar limb scattering radiation, which is then retrieved to obtain the distribution of the ozone profile with a height of 10–60km. The absorption bands of ozone in the UV band are mainly Hartley and Huggins bands with a peak absorption wavelength of nearly 300 nm. The absorption band of ozone in the VIS band is mainly Chappuis band with a peak absorption wavelength of around 602 nm. The NIR band is mainly used to remove the influence of aerosol [5–6].

#376043 https://doi.org/10.1364/OE.27.031348
Journal © 2019 Received 26 Aug 2019; revised 1 Oct 2019; accepted 7 Oct 2019; published 14 Oct 2019

Hyperspectral imaging technology is a new space optical remote sensing technology based on multispectral imaging. With hyperspectral imaging technology, the image and spectral information of the target can be obtained simultaneously. Such technology plays an increasingly important role in land, sea, and atmosphere remote sensing [7–8]. The limb hyperspectral imager for ozone detection is a new space optical remote sensing instrument with important research and application value for the use of imaging spectrometry to explore the atmosphere. The Shuttle Ozone Limb Sounding Experiment (SOLSE) uses a filter wheel to rotate the ultraviolet and visible filters to achieve time-sharing detection in the ultraviolet and visible bands [9–11]. The disadvantage is that the detection of the ultraviolet and visible bands is not synchronized, and the retrieval accuracy is low. The brightness signal in the ultraviolet band is 2 to 3 orders of magnitude weaker than the brightness signal in the visible band. In the range of ultraviolet to visible to near infrared, the dynamic range of the brightness signal reaches the range of 10^5, while the dynamic range of the CCD itself is only 5×10^4, so how to achieve wide-band, large dynamic range limb imaging spectroscopy simultaneous detection is one of the keys to the design and development of wide-band limb ozone profile instrument. The Scanning Imaging Atmospheric Absorption Mapping Instrument (SCIAMACHY) developed by ESA uses multiple color separation films to divide into multiple channels to achieve simultaneous detection of wide-band, large dynamic range limb imaging spectral detection [12], but its disadvantage is that there are many channels. It is bulky and heavy and cannot be miniaturized.

In this paper, a new method for adjusting the intensity of incident signals with band attenuation filter to achieve simultaneous detection of wide-band, large dynamic range limb imaging spectrum is proposed. The optical system design of the prism dispersion type wide-band limb hyperspectral imager was completed, and the design and measurement results were analyzed and evaluated.

2. Application requirements and specifications

The spectrometer requires the spectral resolution of the instrument to correspond to the absorption properties of ozone. As the wavelength increases, the absorption band of ozone should be widened. The working band of the instrument is 280–1000 nm, the detection range of limb height is 10–60 km, and the field of view coverage is 10–90 km. In the limb height direction, the spatial resolution (GSD) is 3 km. The signal-to-noise is large than 20 over the full spectral range. The pixel size of the selected detector is 13 μm × 13 μm, the pixel number is 1024 (spectral dimension) × 1024 (spatial dimension), the four pixels are combined in spatial dimension, and four pixels are combined in spectral dimension.

Table 1. Specifications of spectrometer

Parameters	Values
Spectral range /nm	280–1000nm
Field of view /(°)	2.4°×0.02°
Focal length of telescope f'_t /mm	69
Focal length of system f's /mm	69
Diameter of entrance pupil /mm	10
Detector array size /pixel	1024 ×1024
Detector pixel size /μm	13×13 (4×4 binning)
Spectral resolution /nm	1 nm@280 nm
	25nm@1000 nm
Modulation transfer function	≥0.5@9.6 lp/mm
Volume	≤350mm×230mm×90mm
Weight	≤10.5kg

The orbital height H is calculated at 400 km. The center of the instrument is located at the edge of 50 km. The distance L between the limb hyperspectral imager and the limb observation point is 2149.9km. The main technical specificaitons of the optical system are shown in Table 1.

3. Optical design

The limb hyperspectral imager detects a wide band and a large dynamic range of signals. Figure 1 shows the relationship between the spectral radiance of the Earth's limb and the limb height obtained by the MORTRAN software. It can be seen that the signal in the ultraviolet band is weak, the signal in the visible and near-infrared bands is large. In the working band, the limb spectral radiance changes to 10^5. In order to ensure that the weak UV signal can be detected, the large signals in the visible and near-infrared bands are not saturated on the CCD detector, and a band-attenuation filter is placed in front of the telescope. The intensity of the incident signal is adjusted such that the adjusted signal is within the dynamic range of the CCD detector. Figure 2 is a transmission curve of a band-attenuating filter that can be implemented using existing coating techniques. The optical system of limb hyperspectral imager consists of a telescope system and a spectral imaging system, which are connected together by an entrance slit. Atmospheric radiation from the Earth's limb is imaged on the entrance slit by the telescope system. The entrance slit can be regarded as the object of the spectral imaging system. The incident slit is imaged by the spectral imaging system on the CCD detector. The length of the slit image is the spatial dimension, and the dispersion direction is the spectral dimension. The limb hyperspectral imger detects a wide band, and the spectral resolution needs to match the absorption characteristics of ozone, the spectral resolution of the ultraviolet band is high, and the spectral resolution of the visible and near-infrared bands is low. Therefore, the prismatic dispersive spectral imaging system is selected. and the dispersion nonlinearity of the prism coincides with the characteristics required by the spectral resolution specifications.

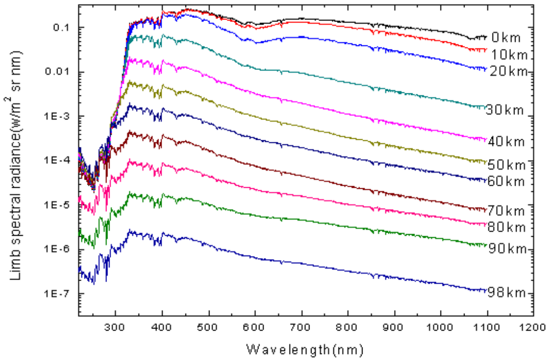

Fig. 1. Curve of limb spectral radiance

Figure 3 shows the spectral efficiency or transmission of the instrument including transmission and reflective efficiency of optical elements, quantum efficiency of CCD, the total throughput of optical system, and the total throughput of the instrument. Figure 4 shows the number of signal electrons on one pixel of the CCD over the full spectral range for different limb height. The CCD47-20 of E2V company is used, and the peak charge storage is 100000 e-/ pixel. The maximum number of signal electrons on one pixel. is 86300 e-/ pixel, which is less than the peak charge storage the CCD, so the CCD is not saturated for the maximum signal. The minimum signal is large than 100 e-/ pixel. The 6×4 pixels are binning. Figure 5 shows the signal-to-noise of the instrument over the full spectral range for different limb height, and the

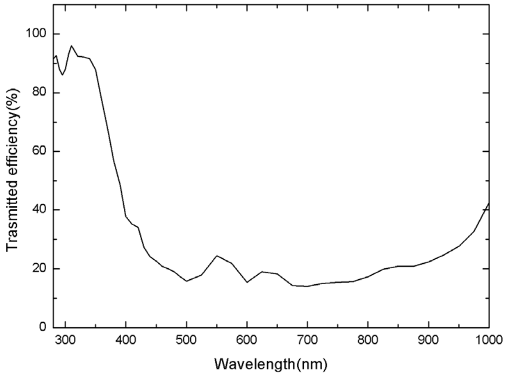

Fig. 2. The designed transmitted efficiency curve of the filter

minimum signal-to-noise is large than 20. Thereby the special filter enables to capture the full dynamic range without saturation and sufficient signal-to-noise.

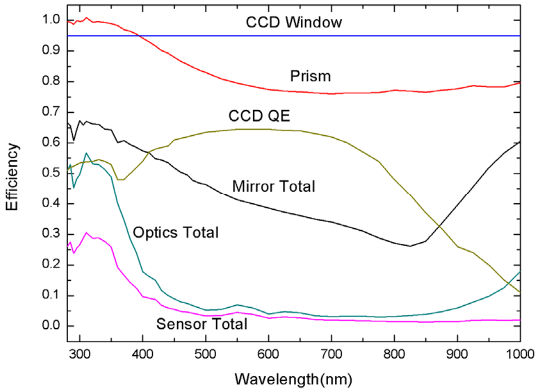

Fig. 3. Spectral efficiency or transmission of the instrument

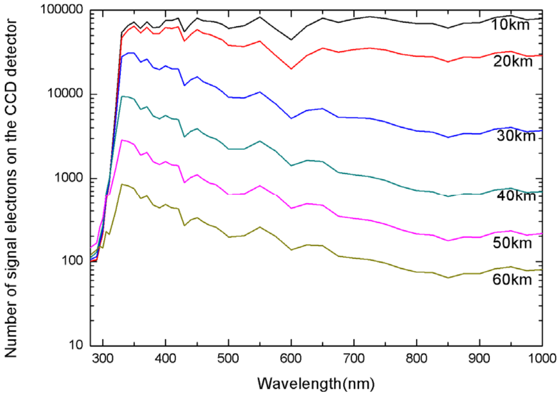

Fig. 4. Number of signal electrons on one pixel on the CCD

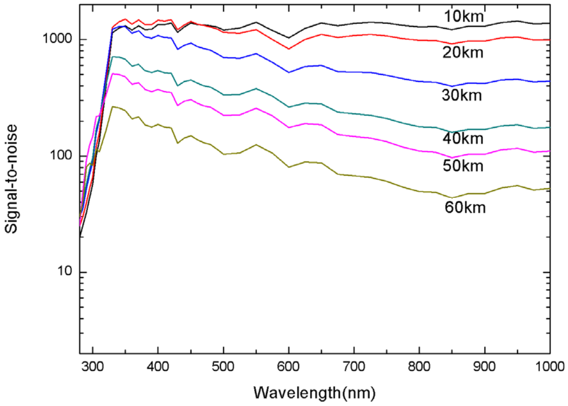

Fig. 5. Signal-to-noise of the over the full spectral range

3.1. Design of the telescope system

The role of the telescope system is to image the Earth's limb atmospheric radiation on the entrance slit. The working wavelength range is 280nm~1000 nm. The working waveband is wide, covering the ultraviolet, visible and near-infrared bands. The field of view is 2.4°×0.02°, and the focal length f'_t is 69 mm and the relative aperture is 1/6.9. In principle, the telescopic system can adopt a transmissive structure and a reflective structure [13–16]. However, due to the wide working band and the small number of materials that can be selected in the ultraviolet band, it is difficult to correct the chromatic aberration of the transmissive structure. The reflective structure can work in a wide band while avoiding the influence of chromatic aberration. In order to maximize energy efficiency, the telescope system adopts a single off-axis parabolic mirror structure. Figure 6 is the spot diagram on the image plane of the telescope system. The Root Mean Square (RMS) radius is less than 1/2 equivalent pixel, which satisfies the imaging quality requirements.

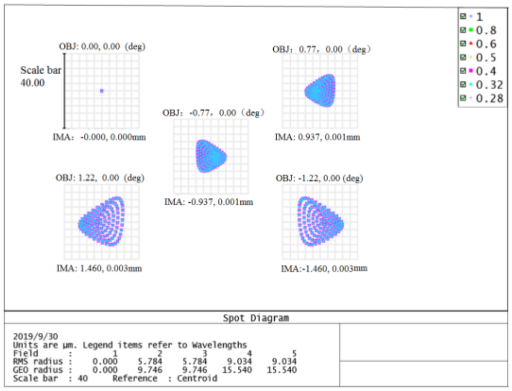

```
2019/9/30
Units are µm. Legend items refer to Wavelengths
Field       :        1        2        3        4        5
RMS radius  :    0.000    5.784    5.784    9.034    9.034
GEO radius  :    0.000    9.746    9.746   15.540   15.540
Scale bar   : 40      Reference   : Centroid
```

Fig. 6. Spot diagram on the image plane of telescope

3.2. Design of the spectral imaging system

The function of the spectral imaging system is to image the image formed by the telescope system on the entrance slit through the dispersion on the image surface of the CCD detector. [17–19]. The spectral resolution of the limb hyperspectral imager is determined by the spectral imaging system, and the spatial resolution is also closely related to the imaging quality of the spectral imaging system. The spectral imaging system uses a dispersive prism as a dispersive element. The refractive index of the prism changes with wavelength, so under the same incident angle, the exit angle varies with wavelength. Because the covered band is wide and contains the ultraviolet band, the dispersive prism is made of fused silica. The entrance slit has a size of 2.9 mm× 0.045 mm, a numerical aperture of 0.07, and a zoom ratio of 1/1. The typical optical structure of the prismatic dispersive spectral imaging system is the Off-Axis Spherical surface Spectral Imaging System (OASIS) [20]. A large-aperture correction lens is required to be interspersed in the collimated and dispersive optical paths. The large-aperture correction lens is heavy and has some difficulties to make. According to the requirements of miniaturization and light weight, we improve the Off-axis Spherical surface Spectral Imaging System. On the one hand, the collimating mirror and the imaging mirror are replaced by aspheric surfaces, and the large-aperture correction lens is eliminated. On the other hand, the second working surface of the dispersive prism is directly plated with an internal reflection film, and the Litrow mirror is eliminated. The optical structure of the improved off-axis aspheric surface spectral imaging system is as shown in Fig. 10, and the light emitted from the entrance slit is folded through the plane mirror. After being folded, the light is incident on the aspheric collimating mirror, collimated by the aspheric collimating mirror, and then incident on the first working surface of the dispersing prism, then being reflected by the second working surface, and exit from the first working surface. The dispersive beam is focused by an aspherical focusing mirror onto the CCD detector.

Figure 7 shows the positional distribution of image points for different wavelengths on the image plane. Figure 8 shows the RMS spot radius VS wavelength. In the whole working band, the maximum value of RMS spot radius is 6.5µm, which is less than half the size of the detector. Therefore, the imaging quality is high in the entire working band.

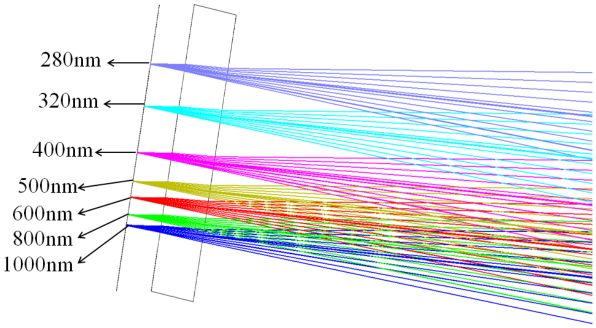

Fig. 7. The positional distribution of image points for different wavelengths on the image plane.

When the entrance slit width W_s is 0.052 mm, the magnification of the spectral imaging system is 1/1. The ideal width of the slit image W_s' is 0.052 mm. However, considering the influence of aberration, the actual width of the slit image W_e is

$$w_e = \sqrt{w_s'^2 + D^2} = 0.054\text{mm}. \tag{1}$$

In the formula above, the RMS value for the diameter of the dispersion direction $D = 13\mu\text{m}$. Spectral resolution of the spectral imaging system $\Delta\lambda$ is

$$\Delta\lambda = \left(\frac{d\lambda}{dl}\right) \times w_e. \tag{2}$$

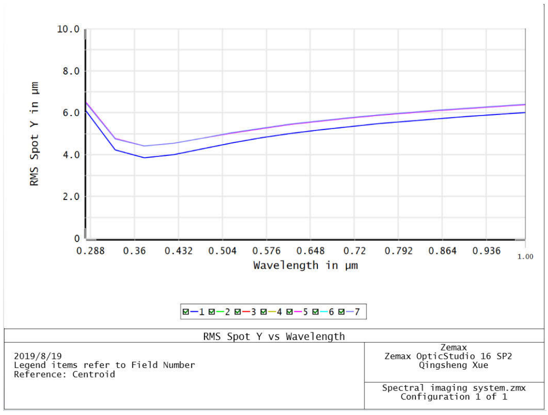

Fig. 8. The RMS spot radius VS wavelength

In the formula above, $d\lambda/dl$ is the reciprocal of the line dispersion rate. The refractive index of fused quartz meets the Sellmeier formula with the change in the wavelength.

$$n = \sqrt{1 + \frac{K_1\lambda^2}{\lambda^2 - L_1} + \frac{K_2\lambda^2}{\lambda^2 - L_2} + \frac{K_3\lambda^2}{\lambda^2 - L_3}}. \tag{3}$$

In the formula above, K_1=6.96166300E-001, L_1=4.67914800E-003, $K_2 = 4.07942600\text{E-}001$, L_2=1.35120630E-002, K_3=8.97479400E-001, L_3=9.79340025E + 001. The top angle of the fused quartz dispersion prism α is 15.3°. The deviation angle of the dispersion prism δ is

$$\delta = i_1 + \arcsin\left[n\sin\left(2\alpha - \arcsin\frac{\sin i_1}{n}\right)\right] - 2\alpha. \tag{4}$$

We consider i_1 as the incident angle of light across the dispersion prism. Given the differential of the wavelength from formula (4), we can ascertain that

$$\frac{d\delta}{d\lambda} = \frac{\sin\left[2\alpha - \arcsin\left(\frac{\sin i_1}{n}\right)\right]}{\sqrt{1 - n^2\sin^2\left[2\alpha - \arcsin\left(\frac{\sin i_1}{n}\right)\right]}}\cdot\frac{dn}{d\lambda} + \frac{\sin i_1 \cdot \cos\left[2\alpha - \arcsin\left(\frac{\sin i_1}{n}\right)\right]}{\sqrt{n^2 - \sin^2 i_1}\cdot\sqrt{1 - n^2\sin^2\left[2\alpha - \arcsin\left(\frac{\sin i_1}{n}\right)\right]}}\cdot\frac{dn}{d\lambda} \tag{5}$$

Thus, the line dispersion rate of the spectral imaging system is

$$\frac{dl}{d\lambda} = \frac{f}{\cos\sigma}\cdot\frac{d\delta}{d\lambda}. \tag{6}$$

We integrate σ=1.464° into the formula above for the tilt angle of the detector. f is the focal length of the focusing mirror. From formulas (1)–(6), we can determine the relation curve of spectral resolution with wavelength. Figure 9 shows the required and designed spectral resolution. It is clearly that the designed spectral resolution is better than the required index.

3.3. Complete system design of hyperspectral imager

The optical structure of the whole system of the limb hyperspectral imager is connected by the optimized telescope system and the spectral imaging system as shown in Fig. 10. In the spatial direction, four pixels are combined, the equivalent pixel size is 52µm, and the corresponding

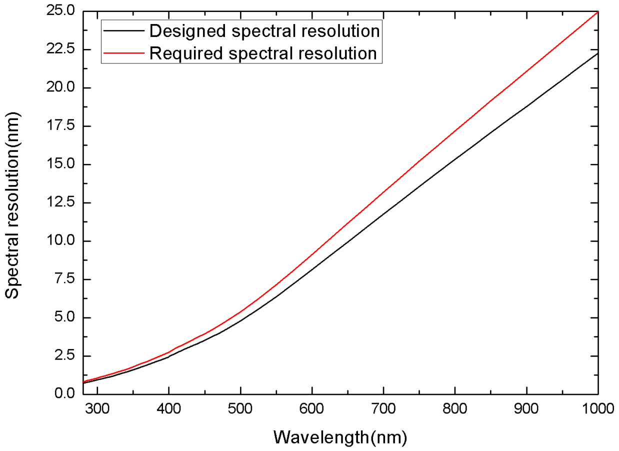

Fig. 9. The required and designed spectral resolution

characteristic frequency is 9.6lp/mm. The optical transfer function curve of different wavelengths of the hyperspectral imager is shown in Fig. 11. It can be seen that at the characteristic frequency, the optical transfer function is greater than 0.68, which is superior to the optical design index requirement. The volume of the entire optical system is 310mm×220mm×70mm, and the quality of the whole instrument can be controlled within 10kg.

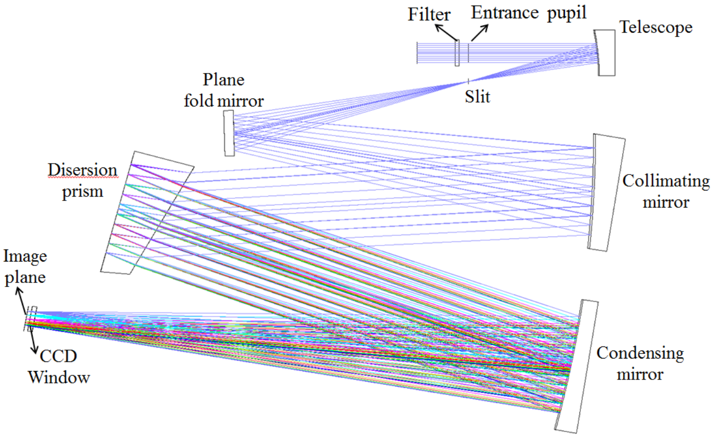

Fig. 10. Optical path of limb hyperspectral imager

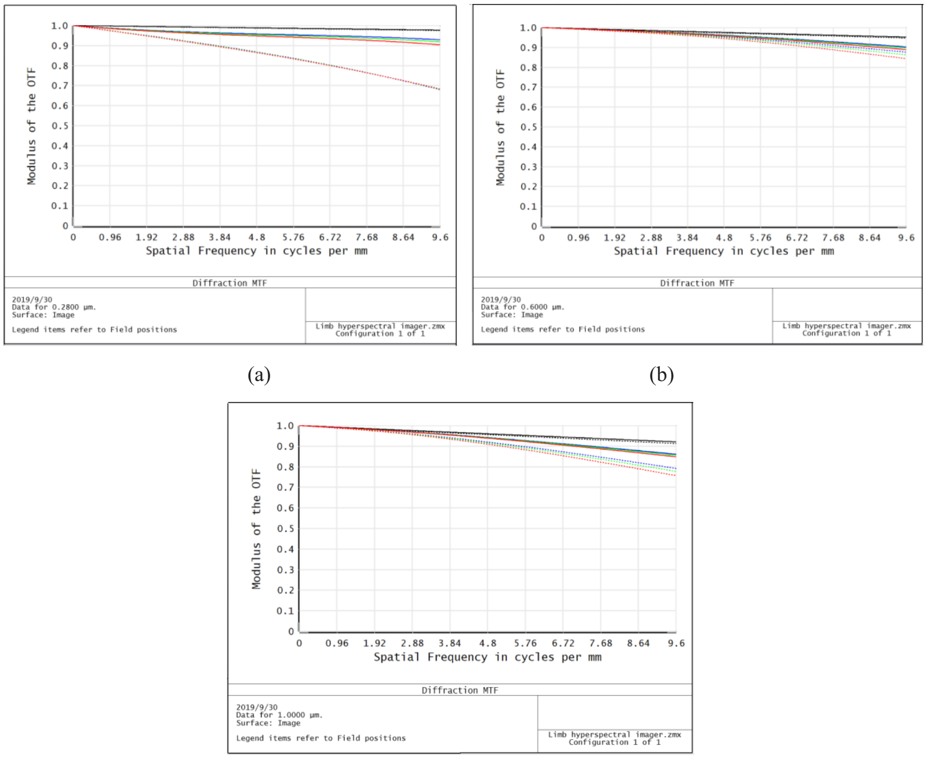

(a)

(b)

(c)

Fig. 11. MTF of limb hyperspectral imager for different wavelengths (a) 280 nm, (b) 600 nm, (c) 100nm

4. System integration and testing

According to the optical design results, the mechanical structure design was completed. The mechanical structure model is shown in Fig. 12. Figure 13 shows the spectral efficiency curve of the special filter and optical system, including the designed and the measured value. It can be seen from Fig. 13 that the measured throughput of the optical system is very close to the design value, which meets the application requirements.

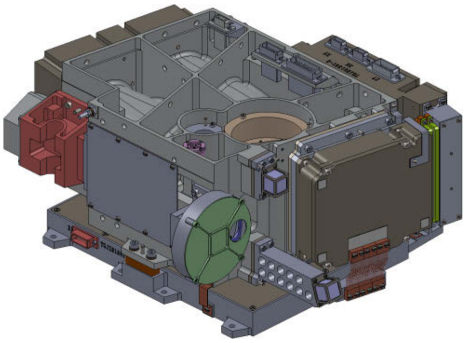

Fig. 12. The mechanical structure model

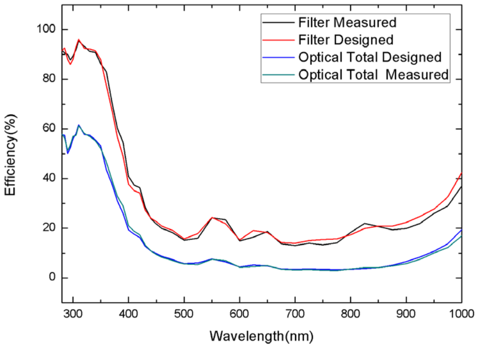

Fig. 13. The comparison of the measured and designed efficiency

The designed spot size of the telescope is 9.03 μm. After adjustment of the telescope system, the measured spot size is 12 μm, which meets the imaging quality requirements. Figure 14 shows the process of high-precision adjustment of the spectral imaging system. Both the collimating mirror and the imaging mirror are off-axis aspherical mirrors, however they have a common main optical axis, so they can be adjusted by a common reference, namely the standard plane lens of Zygo interferometer. The high-precision adjustment of the spectral imaging system is completed by the common reference adjustment method.

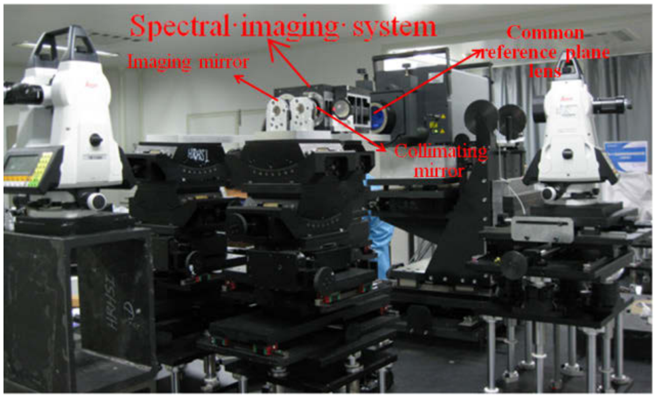

Fig. 14. The integration of spectral imaging system

Figure 15 shows the designed wavefront aberration of the spectral imaging system, which is 0.234 λ, Fig. 16 shows the actual measured wavefront aberration, which is 0.252λ. It is close to the designed wavefront aberration shown in Fig. 15, thereby indicating that the spectral imaging system achieves good imaging quality.

Figure 17 shows the designed and measured spectral resolution. It is clearly that the measured spectral resolution is closed to the designed resolution, and meets the design requirements. The photo of the limb hyperspectral imager is shown in Fig. 18. Figure 19 shows the spectral image of the mercury lamp measured in the laboratory, The central wavelengths in the order from left to right is 296.7nm, 365nm, 404.7nm, 435.8nm, 546.1nm, 578nm and 690.7 nm. On September 15th, 2016, the limb hyperspectral imager on China's Tiangong-2 spacecraft was launched, and the atmospheric limb spectral image data was obtained on the orbit.

Figure 20 is a plot of the limb spectral radiance obtained in the orbit with the limb height and wavelength. As shown in Fig. 20, the abscissa is the wavelength and the ordinate is the limb

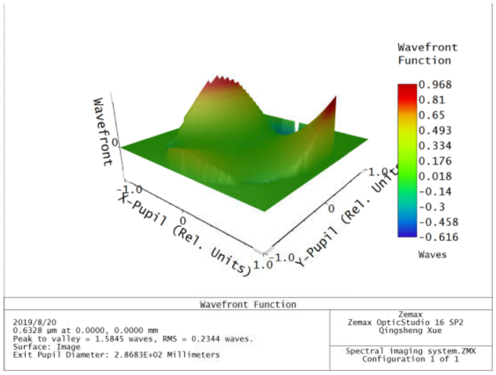

Wavefront Function

2019/8/20
0.6328 µm at 0.0000, 0.0000 mm
Peak to valley = 1.5845 waves, RMS = 0.2344 waves.
Surface: Image
Exit Pupil Diameter: 2.8683E+02 Millimeters

Zemax
Zemax OpticStudio 16 SP2
Qingsheng Xue

Spectral imaging system.ZMX
Configuration 1 of 1

Fig. 15. The designed wavefront aberration

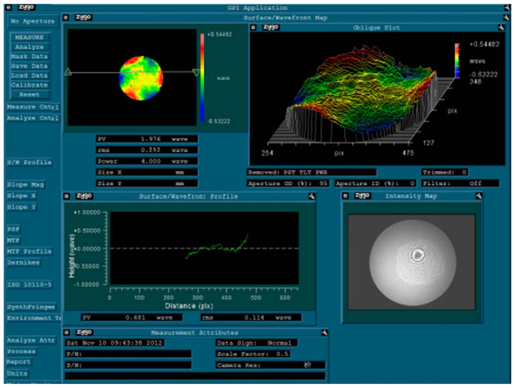

PV 1.976 wave
rms 0.252 wave
Power 4.000 wave
Size X mm
Size Y mm
Removed: PST TLT PWR
Trimmed: 0
Aperture OD (%): 95
Aperture ID (%): 0
Filter: off
PV 0.681 wave
rms 0.114 wave
Sat Nov 10 09:43:38 2012
Data Sign: Normal
P/N:
Scale Factor: 0.5
S/N:
Camera Res:

Fig. 16. The actual measured wavefront aberration

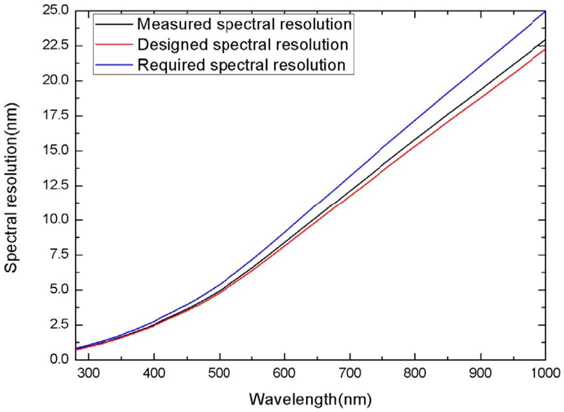

Fig. 17. The required and measured spectral resolution

Fig. 18. The photo of the limb hyperspectral imager

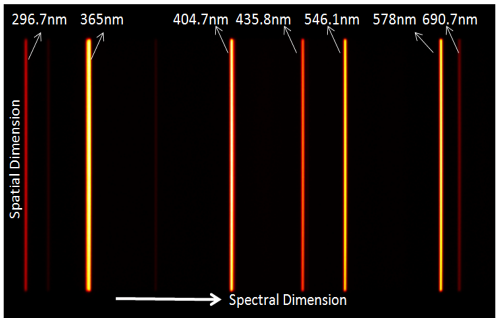

Fig. 19. Mercury lamp spectrum image in laboratory

height and limb spectral radiance. It can be seen that the spectral radiance of different limb height is different, and the profile distribution of ozone can be retrieved according to the difference of spectral radiance. As shown in Fig. 21, we compare the ozone profile retrieved based on in-orbit data measured by the limb sensor developed by us and the Ozone Mapping and Profiler Suite (OMPS) developed by Ball Aerospace & Technologies Corp. The relative deviation of the ozone retrieval based on the in-orbit data is less than 3%, within the relative deviation range between international same kind of instruments, therefore the in-orbit performance of the instrument is excellent apparently.

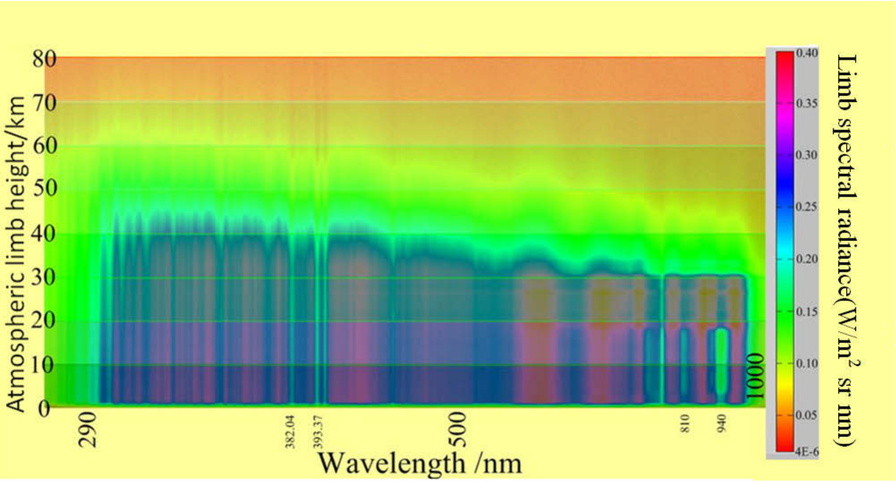

Fig. 20. On-orbit limb spectral images

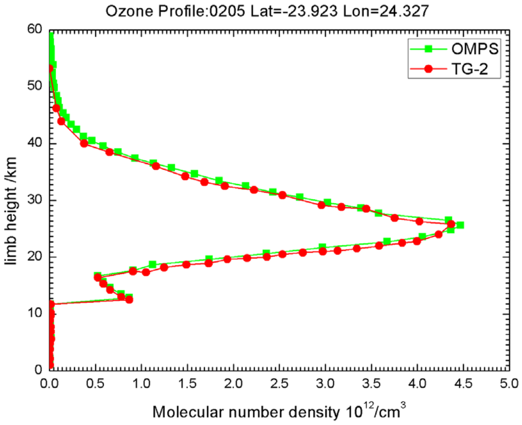

Fig. 21. Ozone profile based TianGong-2 and OMPS

5. Conclusion

According to the requirements of wide band, large dynamic range and miniaturization, a new method is proposed by using of band-attenuation filter to realize simultaneous detection of wide-band large dynamic range limb spectral imaging. A prismatic dispersion spaceborne limb hyperspectral imager for ozone detection is designed and developed. The hyperspectral imager can provide the limb hyperspectral radiances images with wide-band and large dynamic range. It is composed of off-axis parabolic telescope and prism dispersive off-axis aspheric spectrometer. The spectral range is from 280nm to 1000nm, the field of view is 2.4° (limb vertical direction) × 0.02° (horizontal direction), and the focal length is 69mm. The design results meet the requirements of image quality with the characteristics of small volume and light weight, thereby making it especially suitable for the application of space remote sensing unlike existing methods that utilize complicated scanning mirror and multiple color separators. The limb hyperspectral imager is measured and calibrated on ground. It detected limb hyperspectral radiances on Tiangong-2 spacecraft of China. This wide-band hyperspectral imager design can also be applied to terrestrial and marine hyperspectral remote sensing observations.

Funding

National Key Research and Development Program of China (2016YFB0500300, 2016YFB0500301, 2016YFB0500302, 2016YFB0500303, 2016YFB0500304); Jilin Scientific and Technological Development Program (20190302083GX); National Natural Science Foundation of China (41105014, 41527806, 41575023).

References

1. X. H. Wang and Q. S. Xue, “Optical system design of an atmospheric detector with nadir view and omnidirectional limb view,” Appl. Opt. **56**(26), 7454–7461 (2017).
2. Q. S. Xue and M. Z. Duan, “Development of limb imaging spectrometer for atmospheric trace gas sounding,” J,” Acta Opt. Sin. **33**(5), 0522001 (2013).
3. Y. Yamamoto, A. Kuze, T. Kawashima, K. Shibasaki, M. Suzuki, T. Sano, and T. Ogawa, “Conceptual design of the Ozone Dynamics Ultraviolet Spectrometer (ODUS) on the Global Change Observation Mission (GCOM)-A1 satellite,” Proc. SPIE **4135**, 160 (2000).
4. P. F. Levelt, G. H. J. van der Oord, M. R. Dobber, A. Mälkki, H. Visser, J. de Vries, P. Stammes, J. O. V. Lundell, and H. Saari, “The ozone monitoring instrument,” IEEE Trans. Geosci. Electron. **44**(5), 1093–1101 (2006).
5. J. W. Leitch, J. V. Rodriguez, and M. Dittman, “Limb scatter ozone profiling sensor for the NPOESS ozone mapping and profiler suite (OMPS),” Proc. SPIE **4891**, 13–21 (2003).
6. M. G. Dittman, J. Leitch, and M. Chrisp, “Limb broad-band imaging spectrometer for the NPOESS ozone mapping and profiler suite (OMPS),” Proc. SPIE **4814**, 120–130 (2002).
7. E. Dekemper, D. Fussen, B. V. Opstal, J. Vanhamel, D. Pieroux, F. Vanhellemont, N. Mateshvili, G. Franssens, V. Voloshinov, C. Janssen, and H. Elandaloussi, “ALTIUS: a spaceborne AOTF-based UV-VIS-NIR hyperspectral imager for atmospheric remote sensing,” Proc. SPIE **9241**, 92410L (2014).
8. Y. Dobrolenskiy, I. Dziuban, Y. Ivanov, I. Syniavskyi, D. Ionov, A. Poberovsky, O. Korablev, A. Fedorova, and N. Vyazovetskiy, “Optical design of imaging spectrometer for atmosphere monitoring from near-Earth orbit,” Proc. SPIE **10690**, 75 (2018).
9. R. D. McPeters, S. J. Janz, E. Hilsenrath, T. L. Brown, D. E. Flittner, and D. F. Heath, “The retrieval of O3 profiles from limb scatter measurements: Results from the Shuttle Ozone Limb Sounding Experiment,” Geophys. Res. Lett. **27**(17), 2597–2600 (2000).
10. D. E. Flittner, P. K. Bhartia, and B. M. Herman, “O3 profiles retrieved from limb scatter measurements,” Geophys. Res. Lett. **27**(17), 2601–2604 (2000).
11. R. D. McPeters, S. J. Janz, and E. Hilsenrath, “The retrieval of O3 profiles from limb scatter measurements: Resuluts from the Schuttle ozone limb Sounding experiment,” Geophys. Res. Lett. **27**(17), 2597–2600 (2000).
12. M. van Meele, R. J. vander, and J. van Geffen, “Space-based surface UV monitoring for Europe using SCIAMACHY and MSG,” Proc. SPIE **5979**, 59791K (2005).
13. A. Hammar, O. M. Christensen, W. Park, S. Pak, A. Emrich, and J. Stake, “Stray light suppression of a compact off-axis telescope for a satellite-borne instrument for atmospheric research,” Proc. SPIE **10815**, 15 (2018).
14. A. Hammar, W. Park, S. Chang, S. Pak, A. Emrich, and J. Stake, “Wide-field off-axis telescope for the Mesospheric Airglow/Aerosol Tomography Spectroscopy satellite,” Appl. Opt. **58**(6), 1393–1399 (2019).
15. D.-U. Rufino, “Medium-precision null-screen testing of off-axis parabolic mirrors for segmented primary telescope optics: the Large Millimeter Telescope,” Appl. Opt. **39**(16), 2790–2804 (2000).
16. S. Chang, “Off-axis reflecting telescope with axially-symmetric optical property and its applications,” Proc. SPIE **6265**, 626548 (2006).
17. M. A. Folkman, J. Pearlman, L. B. Liao, and P. J. Jarecke, “EO-1/Hyperion hyperspectral imager design, development, characterization, and calibration,” Proc. SPIE **4151**, 40–51 (2001).
18. P. R. Silverglate and D. E. Fort, “System design of the CRISM (compact reconnaissance imaging spectrometer for Mars) hyperspectral imager,” Proc. SPIE **5159**, 283 (2004).
19. Y. Kim, J. Hong, B. Choi, J.-U. Lee, Y. Kim, and H. Kim, “Assembly and alignment method for optimized spatial resolution of off-axis three-mirror fore optics of hyperspectral imager,” Opt. Express **25**(17), 20817–20828 (2017).
20. F. Blechinger, B. Harnisch, and B. Kunkel, “Optical concepts for high resolution imaging spectrometers,” Proc. SPIE **2480**, 165–179 (1995).